J. Fluid Mech. (2020), *vol.* 898, A20. © The Author(s), 2020.
Published by Cambridge University Press
doi:10.1017/jfm.2020.397

Electrokinetically enhanced cross-stream particle migration in viscoelastic flows

Akash Choudhary[1], Di Li[2], T. Renganathan[1], Xiangchun Xuan[2,†] and S. Pushpavanam[1,†]

[1]Department of Chemical Engineering, Indian Institute of Technology Madras, TN 600036, India

[2]Department of Mechanical Engineering, Clemson University, SC 29634-0921, USA

(Received 6 October 2019; revised 23 April 2020; accepted 14 May 2020)

Advancements in understanding the lateral migration of particles have helped in enhanced focusing in microfluidic devices. In this work, we investigate the effects of electrokinetics on particle migration in a viscoelastic flow, where the electric field is applied parallel to the flow. Through experiments and use of perturbation theory in conjunction with the reciprocal theorem, we show that the interaction of electrokinetic and rheological effects can result in an enhancement in migration by an order of magnitude. The theoretical analysis, in agreement with the experiments, demonstrates that the particles can be focused at different equilibrium positions based on their intrinsic electrical properties.

Key words: microfluidics, viscoelasticity

1. Introduction

In the past two decades, biological and healthcare research has significantly benefited by the application of various particle and cell sorting techniques – inertial focusing (Di Carlo 2009; Warkiani *et al.* 2015; Zhang *et al.* 2016) and viscoelastic focusing (Leshansky *et al.* 2007; Lu *et al.* 2017) – in microfluidic devices. The working principle of such devices is based on the exploitation of nonlinearity in the flow (arising from inertial or polymeric stresses) which breaks the symmetry and generates a lateral force on the particle, pushing it towards the equilibrium positions. Since most biological fluids are non-Newtonian, it is essential to understand the rheological effects on particle migration. The pioneering studies of Mason and his coworkers (Karnis & Mason 1966; Gauthier, Goldsmith & Mason 1971) and Ho & Leal (1976) clearly demonstrated that the presence of polymer chains in the fluid exert a normal stress on the particle, pushing it towards the region of lowest shear. In biological fluids, strands of DNA enact the role of polymeric chains and help in the lateral migration of cells (Kim & Kim 2016). In recent years, this normal stress induced migration has been exploited to design tubular-viscoelastic-focusers, in which the region of lowest shear is the channel axis (D'Avino, Greco & Maffettone 2017). However, the labour-intensive fabrication process limits the accessibility of these devices (Nam *et al.* 2015). The more readily available rectangular microchannels

† Email addresses for correspondence: xcxuan@clemson.edu, spush@iitm.ac.in

https://doi.org/10.1017/jfm.2020.397 Published online by Cambridge University Press

are plagued by the limitation of multiple equilibrium positions (one centre and four corners), which renders the downstream detection and separation difficult (Lu *et al.* 2017; Tian *et al.* 2019). Furthermore, the passive nature of the migration requires large focusing lengths which are dependent on the flow rate (D'Avino *et al.* 2017).

Unlike flows at large scale, in microscale flows, the short-ranged effects near the particle surface can determine their fate (Datt *et al.* 2017). One can resort to manipulation of surface effects through external fields to tune particle focusing (Rossi *et al.* 2019). This has potential applications in focusing, separation and detection of rare circulating tumour cells in the blood stream (Zhang *et al.* 2014). Recent studies have shown that cancer cells exhibit a highly negative charge on their surface which can be used to separate them from the bloodstream by applying external electric fields (Chen *et al.* 2016; Le *et al.* 2019). In our previous study (Choudhary, Renganathan & Pushpavanam 2019), we studied the effects of electric fields on the inertial migration in pressure driven flow of a Newtonian fluid. Since most biological fluids exhibit non-Newtonian behaviour, it is important to understand the influence of electrokinetics on the migration in complex fluids.

In this work, we experimentally and theoretically investigate the influence of electrophoresis on viscoelastic focusing of particles, where the electric field is applied parallel to the flow. A vast majority of cells and particles, when submerged in aqueous electrolytes, acquire a surface charge which attracts the counter-charged ions. As a result a thin double layer forms around the particle (Anderson 1989). An external electric field causes a tangential slip on the surface of the particle. This generates a disturbance field around the particle which may amplify the asymmetry in normal stresses. Our experimental results demonstrate that the focusing is significantly accelerated in the presence of an electric field, which reduces the overall focusing length. Furthermore, the electric field provides an external control over the particle migration and enables charge-selective focusing. We explain the experimental observations qualitatively and quantitatively using an approach based on perturbation theory: we analyse the system in the limit of slow and slowly varying flows and capture the viscoelastic effects using a second-order fluid model (Ho & Leal 1976; Bird, Armstrong & Hassager 1987). This allows us to predict the migration velocity through a perturbation solution. Using the reciprocal theorem we show that the electrophoretic motion of the particle generates additional polymeric stresses which enhance the migration by $O(\kappa^{-1})$, where κ is the particle-to-channel size ratio. The theoretical results (obtained without having to resort to fit any parameter) are found to be in reasonable agreement with the experimental observations.

The rest of this article is organized as follows. In § 2 we describe the experimental conditions and results. The explanation of these results is conducted through a mathematical model which is elaborated in § 3. In § 4 we qualitatively and quantitatively compare the theoretical and experimental results. Key conclusions and potential future directions are described in § 5.

2. Experiments

In our experiments, we use a 2 cm long Polydimethylsiloxane (PDMS) microchannel with a rectangular cross-section of 66×54 μm^2. The electric fields were generated using a high-voltage direct current power supply using a wire connection to electrodes at the channel inlet and outlet. We dissolved polyethylene oxide (PEO) powder (molecular weight $= 2 \times 10^6$ g mol^{-1}, Sigma-Aldrich) into a buffer solution (0.01 mM

https://doi.org/10.1017/jfm.2020.397 Published online by Cambridge University Press

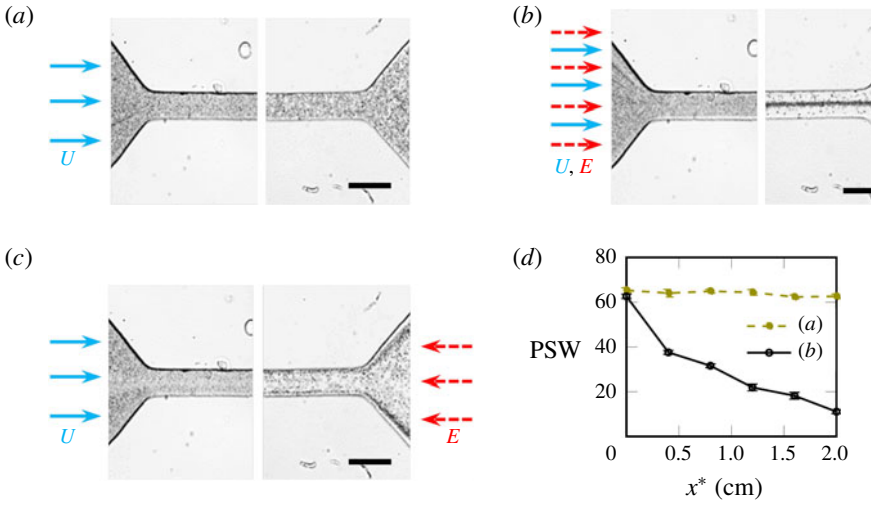


FIGURE 1. Superimposed experimental images showing the focusing of polystyrene particles (negative zeta potential), at the channel inlet and outlet, for: (*a*) no external electric field; (*b*) electric field in the direction of the flow. (*c*) Particle focusing when electric field is applied opposite to the flow. (*d*) Particle stream width for (*a*,*b*). Scale bar represents 100 μm. Parameters: $\mathcal{E}^*_\infty = 300$ V cm^{-1}; $C^*_{PEO} = 250$ ppm; $a^* = 1.1$ μm; $l^* = 66$ μm; $U^*_{max} = 2.9$ mm s^{-1}; $\mu^* = 1.3$ m Pa s; $\zeta^*_p = -83$ mV; $\zeta^*_w = -120$ mV; $Re_p = 1.6 \times 10^{-4}$. Experimental movies corresponding to the above superimposed images can be found as movies 1–6 in the supplementary material, available at https://doi.org/10.1017/jfm.2020.397.

phosphate buffer mixed with 0.5 % Tween 20, Fisher Scientific) at a concentration of 250 ppm. A dilute suspension (<0.1 % in volume fraction) of polystyrene spheres of 2.2 μm diameter is prepared in the PEO solution and is pumped at 25 μl h^{-1}. The particle zeta potential was measured to be −83 mV. Particle motion was visualized at the outlet of the microchannel through an inverted microscope (Nikon Eclipse TE2000U) equipped with a CCD camera (Nikon DS-Qi1MC). Digital videos were recorded at a rate of 15 frames per second, from which the superimposed images were obtained and further processed in the Nikon imaging software (NIS-Elements AR 3.22).

Figure 1(*a*) shows the particles at the inlet and outlet of the channel when no electric field is applied, i.e. the focusing is purely viscoelastic (Karnis & Mason 1966; Gauthier *et al.* 1971; Ho & Leal 1976). The particles remain almost uniformly distributed at the channel exit. This weak focusing is depicted in figure 1(*d*), which shows the change in particle stream width (lateral width of the particle distribution) along the channel length. In figure 1(*b*) an application of an electric field parallel to the flow shows that a significant fraction of the particles are focused at the centreline. Figure 1(*d*) shows that the introduction of an electric field results in substantial reduction in particle stream width. Upon reversing the direction of the electric field (see figure 1*c*), the particles focus near the walls. These results demonstrate the potential to efficiently separate particles and cells based on their intrinsic electrical properties. To extrapolate these observations towards potential applications, it is pivotal to understand the role of electrical properties and flow profile characteristics.

https://doi.org/10.1017/jfm.2020.397 Published online by Cambridge University Press

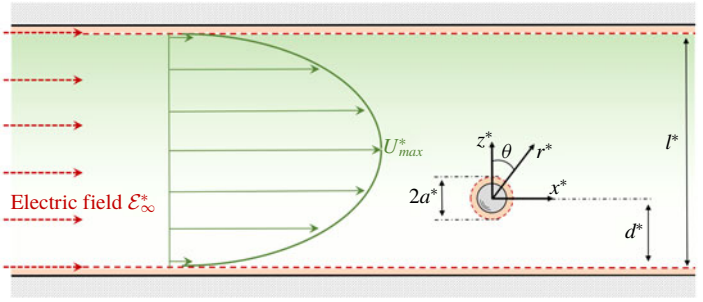


FIGURE 2. Schematic of the problem formulation. The origin of the coordinate system is at the centre of the particle. Here, y^* points in the direction of vorticity of the pressure driven flow. The dashed layer around the particle and walls depicts the outer edge of the double layer. Here, * denotes the dimensional variables.

In what follows, we formulate a mathematical framework to predict, quantify and draw physical insights from the migration behaviour observed in the experiments. Since the particle suspension in the experimental study is dilute, we analyse the migration of a single particle. We model the fluid medium using a second-order fluid (SOF) model (Bird *et al.* 1987), as we are only interested in capturing the effect of small deviations from the Newtonian behaviour. Although the SOF model is only valid for slow and slowly varying (thus nearly Newtonian) flows, it is an asymptotic approximation for most viscoelastic flows (Ho & Leal 1976). Furthermore, it has been shown in the past that dilute PEO solutions ($C^*_{PEO} < 500$ ppm) exhibit pure elastic behaviour (i.e. negligible shear thinning) (Rodd *et al.* 2005; Yang *et al.* 2011; Kim *et al.* 2012). Hence employing the SOF model can help us capture the dynamics in slow Boger fluid flows, both qualitatively and quantitatively.

3. Mathematical model

Figure 2 shows the schematic of a neutrally buoyant electrophoretic sphere suspended in a pressure driven flow of SOF, subjected to a parallel electric field ($\mathcal{E}^*_\infty$). The fluid moves with a maximum velocity of U^*_{max} at the centreline. The frame of reference is placed at the centre of the particle. Typical PDMS microchannel walls and polystyrene particles usually acquire a surface charge (formally quantified as zeta-potential ζ^*) when in contact with an electrolytic solution (Sze *et al.* 2003), which gives rise to an electrical double layer (EDL) (Anderson 1989). In comparison to the channel and particle size, the EDL can be assumed to be asymptotically thin, i.e. $\lambda^*_D/a^* \ll 1$ (where λ^*_D is the EDL thickness). Under the influence of an external electric field, the ions inside the EDL slip in the tangential direction, generating an electro-osmotic slip. For low zeta potentials ($\zeta^*_p \sim 25$ mV), the slip at the particle surface can be represented by Smoluchowski's relation (Keh & Anderson 1985; Anderson 1989). Recently, Ghosh, Chaudhury & Chakraborty (2016) showed that the surface slip in the SOF does not get modified for a surface with constant zeta potential. Hence we employ the Smoluchowski slip in this work.

3.1. *Governing equations*

We represent the system in terms of dimensionless variables, where the coordinates, electrostatic potential, velocity and pressure are non-dimensionalized using a^*, $|\mathcal{E}^*_\infty|a^*$, κU^*_{max} and $\mu^*\kappa U^*_{max}/a^*$, respectively ($\mu^*$ being the dynamic viscosity). Here κ is the

https://doi.org/10.1017/jfm.2020.397 Published online by Cambridge University Press

ratio of particle radius (a^*) to the channel width (l^*). To obtain analytical results, we will later restrict our analysis to small particles ($\kappa \ll 1$), which is consistent with the experimental conditions.

The potential (ϕ) in the electroneutral bulk region is governed by the Laplace equation

$$\nabla^2\phi = 0. \tag{3.1}$$

The boundary conditions at the particle and wall surface (i.e. slip plane of the EDL) are governed by the no-flux condition

$$\boldsymbol{e}_r \cdot \nabla\phi = 0 \quad \text{at } r = 1 \quad \text{and} \quad \boldsymbol{e}_z \cdot \nabla\phi = 0 \quad \text{at } z = -s/\kappa \text{ and } z = (1-s)/\kappa, \tag{3.2a,b}$$

where $s \equiv d^*/l^*$ (as defined in figure 2). The potential is undisturbed ($\phi_\infty \sim -x$) far away from the particle

$$\phi \to \phi_\infty \quad \text{as } r \to \infty. \tag{3.3}$$

The hydrodynamics is governed by the continuity and the Navier–Stokes equations

$$\nabla \cdot \boldsymbol{U} = 0 \quad \text{and} \quad Re_p(\boldsymbol{U} \cdot \nabla \boldsymbol{U}) = \nabla \cdot \boldsymbol{T}, \tag{3.4a,b}$$

where Re_p is particle Reynolds number defined as $\rho^* U^*_{max}\kappa a^*/\mu^*$ (ρ^* being the fluid density). We model the hydrodynamic stress using the second-order-fluid model (Bird *et al.* 1987)

$$\boldsymbol{T} = -P\boldsymbol{I} + \boldsymbol{E}^{(1)} + De\boldsymbol{S}. \tag{3.5}$$

Here, $\boldsymbol{E}^{(1)}$ represents the rate of strain tensor ($\nabla\boldsymbol{U} + \nabla\boldsymbol{U}^\dagger$), $\dagger$ denotes the transpose, $\boldsymbol{S}$ represents the polymeric stress

$$\boldsymbol{S} = \boldsymbol{E}^{(1)} \cdot \boldsymbol{E}^{(1)} + \delta\boldsymbol{E}^{(2)}. \tag{3.6}$$

$\boldsymbol{E}^{(2)}$ is the steady-state covariant convected derivative of $\boldsymbol{E}^{(1)}$ (also known as the Rivlin–Ericksen tensor)

$$\boldsymbol{E}^{(2)} = \boldsymbol{U} \cdot \nabla\boldsymbol{E}^{(1)} + \boldsymbol{E}^{(1)} \cdot \nabla\boldsymbol{U}^\dagger + \nabla\boldsymbol{U} \cdot \boldsymbol{E}^{(1)}. \tag{3.7}$$

Here, De (Deborah number) is the ratio of viscoelastic time scale ($(\Psi_1^* + \Psi_2^*)/\mu^*$) to the time scale corresponding to the average shear in the background flow (l^*/U^*_{max}), δ is a viscometric parameter, Ψ_1^* and Ψ_2^* are the steady shear viscometric coefficients (Bird *et al.* 1987)

$$De = \frac{(\Psi_1^* + \Psi_2^*)U^*_{max}}{\mu^* l^*}, \quad \delta = \frac{-\Psi_1^*}{2(\Psi_1^* + \Psi_2^*)}, \quad \Psi_1^* = \frac{T^*_{xx} - T^*_{zz}}{(\partial U^*_x/\partial z^*)^2}, \quad \Psi_2^* = \frac{T^*_{yy} - T^*_{zz}}{(\partial U^*_x/\partial z^*)^2}. \tag{3.8a–d}$$

Since the migration time scale is much larger than the convective time scale ($a^*/\kappa U^*_{max}$), we analyse the migration in quasi-steady-state (Becker, McKinley & Stone 1996; Choudhary *et al.* 2019). Also, we neglect inertial effects (i.e. $Re_p \ll De$) which leaves the polymeric stress as the sole nonlinearity in the system.

The sphere moves with a translational ($\boldsymbol{U}_s$) and rotational ($\boldsymbol{\Omega}_s$) velocity, which is to be determined from force and torque balance. Since the domain is infinite in the y-direction, we can consider $\boldsymbol{U}_s = U_{sx}\boldsymbol{e}_x + U_{sz}\boldsymbol{e}_z$ and $\boldsymbol{\Omega}_s = \Omega_{sy}\boldsymbol{e}_y$. To account for the electrokinetic effects in the EDL, we employ the slip-boundary condition (Smoluchowski 1903) and impose at the particle surface

$$\boldsymbol{U} = \boldsymbol{\Omega}_s \times \boldsymbol{r} + Ha\zeta_p\nabla\phi \quad \text{at } r = 1. \tag{3.9}$$

https://doi.org/10.1017/jfm.2020.397 Published online by Cambridge University Press

Here, ζ_p is the dimensionless particle surface zeta potential ($\zeta_p^*/|\mathcal{E}_\infty^*|a^*$) and Ha is a Hartmann-type number, $Ha = \varepsilon^*{\mathcal{E}^*}^2_\infty a^*/4\pi\mu^*\kappa U^*_{max}$, which denotes the ratio of electrical energy density to shear stress. Here, ε^* is the electrical permittivity of the medium. Similarly, the flow satisfies the Smoluchowski slip condition at the walls

$$\boldsymbol{U} = Ha\zeta_w\nabla\phi - \boldsymbol{U}_s \quad \text{at walls.} \tag{3.10}$$

As the particle is freely suspended, the translational ($\boldsymbol{U}_s$) and rotational velocity ($\boldsymbol{\Omega}_s$) of the particle are obtained using force-free and torque-free conditions: the total force and torque on the particle must be zero. Apart from the hydrodynamic stress, we also have to account for the Maxwell stress in the calculation of total force and torque. Maxwell stress arises due to a lateral asymmetry in the electrostatic potential distribution around the particle due to the presence of the wall. The Maxwell stress is defined as

$$\boldsymbol{M} = \nabla\phi\nabla\phi - \tfrac{1}{2}(\nabla\phi\cdot\nabla\phi)\boldsymbol{I}. \tag{3.11}$$

It should be noted that there is no contribution from Maxwell stress to the fluid momentum equation (3.4) because $\nabla\cdot\boldsymbol{M} = 0$ in the electroneutral fluid (Yariv 2006). The total force-free and torque-free conditions for particle are given by

$$\boldsymbol{F} = \boldsymbol{F}_H + \boldsymbol{F}_M = \int_{S_p} \boldsymbol{n}\cdot\boldsymbol{T}\,\mathrm{d}S + 4\pi Ha\int_{S_p}\boldsymbol{n}\cdot\boldsymbol{M}\,\mathrm{d}S = \boldsymbol{0}, \tag{3.12a}$$

$$\boldsymbol{L} = \boldsymbol{L}_H + \boldsymbol{L}_M = \int_{S_p} \boldsymbol{n}\times(\boldsymbol{n}\cdot\boldsymbol{T})\,\mathrm{d}S + 4\pi Ha\int_{S_p}\boldsymbol{n}\times(\boldsymbol{n}\cdot\boldsymbol{M})\,\mathrm{d}S = \boldsymbol{0}. \tag{3.12b}$$

Here, subscript H and M represent contributions from hydrodynamic and Maxwell stress, respectively.

3.1.1. *Undisturbed flow*

In the absence of particle, the flow profile for a fully developed pressure driven second-order fluid flow (in the frame of reference of the particle moving with $\boldsymbol{U}_s$) is

$$\boldsymbol{U}_\infty = (\alpha + \beta z + \gamma z^2)\boldsymbol{e}_x + Ha\zeta_w\nabla\phi_\infty - \boldsymbol{U}_s. \tag{3.13}$$

This is identical to that obtained for a Newtonian fluid (Choudhary *et al.* 2019). However, the pressure exhibits a variation in the lateral direction for SOF

$$P_\infty = 2\gamma x + 4De(1+2\delta)(\beta z + \gamma z^2) + \mathcal{I}, \tag{3.14}$$

where $\mathcal{I}$ is an integration constant. The constants α, β and γ are

$$\alpha = 4s(1-s)/\kappa, \quad \beta = 4(1-2s), \quad \gamma = -4\kappa, \tag{3.15a–c}$$

where β and γ represent the shear and curvature of the background flow.

3.2. *Equations governing the disturbance*

We analyse the system in terms of disturbance variables (i.e. deviation from the undisturbed flow). For the different variables, these are defined as: potential ($\psi = \phi - \phi_\infty$), velocity ($\boldsymbol{v} = \boldsymbol{U} - \boldsymbol{U}_\infty$) and pressure ($p = P - P_\infty$). Since the bulk fluid

https://doi.org/10.1017/jfm.2020.397 Published online by Cambridge University Press

medium is electroneutral, the disturbance potential is also governed by the Laplace equation

$$\nabla^2\psi = 0. \tag{3.16}$$

Far away from the particle, ψ decays to zero. Using the definition of disturbance potential in (3.2),

$$\boldsymbol{e_r}\cdot\nabla\psi = -\boldsymbol{e_r}\cdot\nabla\phi_\infty \quad \text{at } r=1 \quad \text{and} \quad \boldsymbol{e_z}\cdot\nabla\psi = 0 \quad \text{at walls.} \tag{3.17a,b}$$

The disturbance flow is governed by continuity and Cauchy's momentum equation

$$\nabla\cdot\boldsymbol{v} = 0 \quad \text{and} \quad \nabla\cdot\boldsymbol{\sigma}_H = \boldsymbol{0}. \tag{3.18a,b}$$

Here, $\boldsymbol{\sigma}_H$ is the hydrodynamic disturbance stress tensor which contains the Newtonian and polymeric contributions ($\boldsymbol{\sigma}_H = -p\boldsymbol{I} + \boldsymbol{e}^{(1)} + De\,\boldsymbol{s}$). Here, $\boldsymbol{I}$ is the identity tensor, $\boldsymbol{e}^{(1)}$ is the rate of strain tensor for the disturbance flow ($\nabla\boldsymbol{v} + \nabla\boldsymbol{v}^\dagger$) and $\boldsymbol{s}$ is the disturbance polymeric stress tensor

$$\boldsymbol{s} = \boldsymbol{e}^{(1)}\cdot\boldsymbol{e}^{(1)} + \boldsymbol{w}^{(1)} + \delta(\boldsymbol{e}^{(2)} + \boldsymbol{w}^{(2)}), \tag{3.19}$$

$$\left.\begin{aligned} \boldsymbol{w}^{(1)} &= \boldsymbol{E}_\infty^{(1)}\cdot\boldsymbol{e}^{(1)} + \boldsymbol{e}^{(1)}\cdot\boldsymbol{E}_\infty^{(1)}, \quad \boldsymbol{e}^{(2)} = \boldsymbol{v}\cdot\nabla\boldsymbol{e}^{(1)} + \boldsymbol{e}^{(1)}\cdot\nabla\boldsymbol{v}^\dagger + \nabla\boldsymbol{v}\cdot\boldsymbol{e}^{(1)}, \\ \boldsymbol{w}^{(2)} &= \boldsymbol{U}_\infty\cdot\nabla\boldsymbol{e}^{(1)} + \boldsymbol{e}^{(1)}\cdot\nabla\boldsymbol{U}_\infty{}^\dagger + \nabla\boldsymbol{U}_\infty\cdot\boldsymbol{e}^{(1)} + \boldsymbol{v}\cdot\nabla\boldsymbol{E}_\infty^{(1)} + \boldsymbol{E}_\infty^{(1)}\cdot\nabla\boldsymbol{v}^\dagger + \nabla\boldsymbol{v}\cdot\boldsymbol{E}_\infty^{(1)}. \end{aligned}\right\} \tag{3.20}$$

Here, $\boldsymbol{E}_\infty^{(1)}$ is the rate of strain tensor for the undisturbed flow, $\boldsymbol{e}^{(2)}$ is the disturbance Rivlin–Eriksen (RE) tensor, $\boldsymbol{w}^{(1)}$ is the 'interaction tensor' (arising from the interaction between background flow and disturbance flow) and $\boldsymbol{w}^{(2)}$ is the RE interaction tensor. Using (3.9) and (3.10), we find that the disturbance flow is subject to the following boundary conditions:

$$\boldsymbol{v} = \boldsymbol{\Omega}_s\times\boldsymbol{r} + Ha\zeta_p\nabla(\psi+\phi_\infty) - \boldsymbol{U}_\infty \quad \text{at } r=1, \tag{3.21a}$$

$$\boldsymbol{v} = Ha\zeta_w\nabla\psi \quad \text{at walls,} \tag{3.21b}$$

$$\boldsymbol{v}\to\boldsymbol{0} \quad \text{as } r\to\infty. \tag{3.21c}$$

The total Maxwell stress can be decomposed into four components as

$$\begin{aligned} \boldsymbol{M} = {} & \left(\nabla\phi_\infty\nabla\phi_\infty - \tfrac{1}{2}(\nabla\phi_\infty\cdot\nabla\phi_\infty)\boldsymbol{I}\right) + \left(\nabla\psi\nabla\phi_\infty - \tfrac{1}{2}(\nabla\psi\cdot\nabla\phi_\infty)\boldsymbol{I}\right) \\ & + \left(\nabla\phi_\infty\nabla\psi - \tfrac{1}{2}(\nabla\phi_\infty\cdot\nabla\psi)\boldsymbol{I}\right) + \left(\nabla\psi\nabla\psi - \tfrac{1}{2}(\nabla\psi\cdot\nabla\psi)\boldsymbol{I}\right). \end{aligned} \tag{3.22}$$

The first term arises from the undisturbed component, the second and third terms denote the contribution from the interaction between applied (ϕ_∞) and disturbed potential field (ψ) and the fourth term denotes the disturbance Maxwell stress. Yariv (2006) showed that the first three components do not result in a net force or torque and the leading-order contribution arises from the fourth term. Since $\boldsymbol{M}$ is divergence free in the fluid domain, only the terms (in (3.22)) decaying as $O(r^{-2})$ contribute to the force (Guazzelli & Morris 2011). Only the disturbance Maxwell stress generates $O(r^{-2})$ terms and provides the leading-order contribution (Yariv 2006, p. 3). Thus, the disturbance Maxwell stress is denoted as

$$\boldsymbol{\sigma}_M = \nabla\psi\nabla\psi - \tfrac{1}{2}(\nabla\psi\cdot\nabla\psi)\boldsymbol{I}. \tag{3.23}$$

Similarly, the undisturbed hydrodynamic field cannot generate a net force or torque on the particle. Hence, the force-free and torque-free conditions are given by

$$\boldsymbol{F} = \boldsymbol{F}_H + \boldsymbol{F}_M = \int_{S_p}\boldsymbol{n}\cdot\boldsymbol{\sigma}_H\,\mathrm{d}S + 4\pi Ha\int_{S_p}\boldsymbol{n}\cdot\boldsymbol{\sigma}_M\,\mathrm{d}S = \boldsymbol{0}, \tag{3.24a}$$

$$\boldsymbol{L} = \boldsymbol{L}_H + \boldsymbol{L}_M = \int_{S_p}\boldsymbol{n}\times(\boldsymbol{n}\cdot\boldsymbol{\sigma}_H)\,\mathrm{d}S + 4\pi Ha\int_{S_p}\boldsymbol{n}\times(\boldsymbol{n}\cdot\boldsymbol{\sigma}_M)\,\mathrm{d}S = \boldsymbol{0}. \tag{3.24b}$$

https://doi.org/10.1017/jfm.2020.397 Published online by Cambridge University Press

3.3. *Migration due to Maxwell stress*

Here we evaluate the force and lateral migration arising from the Maxwell stress (3.23) alone. Since the potential distribution is not affected by the fluid rheology, the Maxwell force on the particle in a second-order fluid is identical to that in a Newtonian fluid (Yariv 2006). Following our previous analysis (Choudhary *et al.* 2019), we use the method of reflections to determine the potential distribution in the particle–wall configuration (Brenner 1962). Since our aim is to obtain qualitative insights and analytical results, we restrict the analysis to small particles i.e. $\kappa \ll 1$. Assuming the small particle is not too close to the walls (i.e. $s \gg \kappa$), the disturbance potential is sought as successive reflections, $\psi = {}_{(1)}\psi + {}_{(2)}\psi + \cdots$. Here, ${}_{(i)}\psi$ represents the ith reflection, where the odd reflections satisfy boundary conditions at the particle surface and the even reflections satisfy the wall boundary conditions. Accounting for each successive pair of reflections increases the accuracy by $O(\kappa)$ (Happel & Brenner 2012, p. 286). Since $\kappa \ll 1$, we take only the first two reflections of disturbance potential into account. Evaluation of $\boldsymbol{F}_M$ and $\boldsymbol{L}_M$ (detailed in § A.2) yields

$$\boldsymbol{F}_M = 4\pi Ha \left(\frac{3\pi}{16}\kappa^4 (\mathfrak{Z}(4, s) - \mathfrak{Z}(4, 1-s)) \right) \boldsymbol{e}_z + O(\kappa^7) \quad \text{and} \quad \boldsymbol{L}_M = \boldsymbol{0}. \tag{3.25a,b}$$

The Maxwell force acts along the cross-stream direction alone and is wall-repulsive in nature; the Maxwell torque is zero. The contribution of Maxwell stresses to the migration velocity is

$$U^M_{mig} \approx \frac{4\pi Ha}{6\pi(1 + O(\kappa))} \left(\frac{3\pi}{16}\kappa^4 (\mathfrak{Z}(4, s) - \mathfrak{Z}(4, 1-s)) \right). \tag{3.26}$$

Here, superscript M shows that the contribution is from Maxwell stress, $\mathfrak{Z}$ is the generalized Riemann zeta function and $6\pi(1 + O(\kappa))$ is the viscous resistance which includes wall correction at the first order (Brenner 1961, p. 246) (the details of evaluation through the method of reflections are provided in the supplementary material). Later we show that U^M_{mig} decays rapidly away from the walls and is negligible in the bulk of the channel, where migration due to hydrodynamic stress dominates.

3.4. *Migration due to hydrodynamic stress*

3.4.1. *Perturbation expansion*

We find the migration at $O(De)$ using a regular perturbation expansion. For small values of De, the disturbance field variables are expanded as

$$\xi = \xi_{(0)} + De\, \xi_{(1)} + \cdots. \tag{3.27}$$

Here, ξ is a generic field variable which represents velocity ($\boldsymbol{v}$), pressure (p), translational ($\boldsymbol{U}_s$) and angular velocity ($\boldsymbol{\Omega}_s$). Since the electrostatic potential is decoupled from the hydrodynamics, the variable ψ is not expanded as in (3.27). We substitute (3.27) in the equations governing the hydrodynamics (3.18)–(3.21). We obtain the problem at $O(1)$ as

$$\left.\begin{gathered} \nabla \cdot \boldsymbol{v}_{(0)} = 0, \\ \nabla^2 \boldsymbol{v}_{(0)} - \nabla p_{(0)} = \boldsymbol{0}, \\ \boldsymbol{v}_{(0)} = \boldsymbol{\Omega}_{s(0)} \times \boldsymbol{r} + Ha\zeta_p \nabla(\psi + \phi_\infty) - \boldsymbol{U}_{\infty(0)} \quad \text{at } r = 1, \\ \boldsymbol{v}_{(0)} = Ha\zeta_w \nabla\psi \quad \text{at walls}, \\ \boldsymbol{v}_{(0)} \to \boldsymbol{0} \quad \text{as } r \to \infty, \end{gathered}\right\} \tag{3.28}$$

https://doi.org/10.1017/jfm.2020.397 Published online by Cambridge University Press

and at $O(De)$ as

$$\left.\begin{array}{c}\boldsymbol{\nabla}\cdot\boldsymbol{v}_{(1)}=0,\\ \nabla^2\boldsymbol{v}_{(1)}-\boldsymbol{\nabla}p_{(1)}=-\boldsymbol{\nabla}\cdot\boldsymbol{s}_{(0)},\\ \boldsymbol{v}_{(1)}=\boldsymbol{U}_{s(1)}+\boldsymbol{\Omega}_{s(1)}\times\boldsymbol{r}\quad\text{at } r=1,\\ \boldsymbol{v}_{(1)}=\boldsymbol{0}\quad\text{at walls},\\ \boldsymbol{v}_{(1)}\to\boldsymbol{0}\quad\text{as } r\to\infty.\end{array}\right\}\tag{3.29}$$

Here, $\boldsymbol{s}_{(0)}$ is the disturbance polymeric stress of $O(De^0)$ field. The angular ($\boldsymbol{\Omega}_s$) and translational velocity ($\boldsymbol{U}_s$) are evaluated by using (3.24), at each order.

3.4.2. *Reciprocal theorem*

The symmetry of Stokes flow implies that the $O(1)$ field cannot produce a lateral lift. Therefore, the lift must arise from the $O(De)$ field. The reciprocal theorem (Ho & Leal 1976) allows us to determine the migration associated with $\boldsymbol{v}_{(1)}$, without having to solve for the $O(De)$ field. The reciprocal theorem relates the properties of an unknown Stokes flow to a known test flow field, provided both flow fields correspond to the same geometry. The test field $(\boldsymbol{u}^t, p^t)$ is chosen to be that generated by a moving sphere in the positive z-direction (towards the upper wall) with unit velocity in a quiescent Newtonian fluid (refer to appendix A for the details of test field). Following Ho & Leal (1976, p. 789), we obtain the lateral migration velocity at $O(De)$ as

$$De(U_{s(1)})_z=U^H_{mig}=-\frac{1}{6\pi(1+O(\kappa))}De\int_{V_f}\boldsymbol{s}_{(0)}:\boldsymbol{\nabla}\boldsymbol{u}^t\,\mathrm{d}V.\tag{3.30}$$

Here, superscript H denotes the hydrodynamic contribution and $6\pi(1+O(\kappa))$ is the viscous resistance including wall correction at the first order (the details of derivation are shown in the supplementary material).

3.4.3. *Evaluation of* $\boldsymbol{v}_{(0)}$

Following the method used for the evaluation of potential (ψ), we use the method of reflections to find the velocity field which satisfies the boundary conditions at the particle and wall surface with sufficient accuracy (Brenner 1962). As in § 3.3, we restrict the analysis to small particles i.e. $\kappa\ll 1$. This condition is in addition to $De\ll 1$, which was used to expand the field variables in (3.27). We seek the disturbance $(\boldsymbol{v}_{(0)}, p_{(0)})$ as

$$\boldsymbol{v}_{(0)}={}_{(1)}\boldsymbol{v}_{(0)}+{}_{(2)}\boldsymbol{v}_{(0)}+\cdots,\quad p_{(0)}={}_{(1)}p_{(0)}+{}_{(2)}p_{(0)}+\cdots.\tag{3.31a,b}$$

Here ${}_{(i)}\boldsymbol{v}_{(0)}$ represents the ith reflection of the creeping flow disturbance velocity. Since $\kappa\ll 1$, we take the first two reflections into account. We substitute the above expansion in the equations governing the creeping flow hydrodynamics (3.28) and obtain the following set of problems:

$$\left.\begin{array}{rcl}\boldsymbol{\nabla}\cdot{}_{(1)}\boldsymbol{v}_{(0)} &=& 0,\quad \nabla^2{}_{(1)}\boldsymbol{v}_{(0)}-\boldsymbol{\nabla}_{(1)}p_{(0)}=\boldsymbol{0},\\ {}_{(1)}\boldsymbol{v}_{(0)} &=& U_{sx(0)}\boldsymbol{e}_x+\Omega_{sy(0)}\boldsymbol{e}_y\times\boldsymbol{r}+Ha\zeta_p(\boldsymbol{\nabla}_{(1)}\psi+\boldsymbol{\nabla}_{(2)}\psi)\\ & & -(\alpha+\beta z+\gamma z^2+Ha(\zeta_p-\zeta_w))\boldsymbol{e}_x\quad\text{at } r=1,\\ {}_{(1)}\boldsymbol{v}_{(0)} &\to& \boldsymbol{0}\quad\text{at } r\to\infty;\end{array}\right\}\tag{3.32}$$

https://doi.org/10.1017/jfm.2020.397 Published online by Cambridge University Press

$$\left.\begin{aligned} \boldsymbol{\nabla}\cdot{}_{(2)}\boldsymbol{v}_{(0)} &= 0, \quad \nabla^2{}_{(2)}\boldsymbol{v}_{(0)} - \boldsymbol{\nabla}{}_{(2)}p_{(0)} = \boldsymbol{0}, \\ {}_{(2)}\boldsymbol{v}_{(0)} &= Ha\zeta_w(\boldsymbol{\nabla}{}_{(1)}\psi + \boldsymbol{\nabla}{}_{(2)}\psi) - {}_{(1)}\boldsymbol{v}_{(0)} \quad \text{at the walls}, \\ {}_{(2)}\boldsymbol{v}_{(0)} &\to \boldsymbol{0} \quad \text{at } r\to\infty. \end{aligned}\right\} \tag{3.33}$$

The first reflection $({}_{(1)}\boldsymbol{v}_{(0)},\ {}_{(1)}p_{(0)})$ is found by employing Lamb's general solution (Lamb 1975; Happel & Brenner 2012)

$$\begin{aligned} {}_{(1)}\boldsymbol{v}_{(0)} = {} & A_1\left(\boldsymbol{e}_x + \frac{x\boldsymbol{r}}{r^2}\right)\frac{1}{r} + B_1\left(-\boldsymbol{e}_x + \frac{3x\boldsymbol{r}}{r^2}\right)\frac{1}{r^3} + C_1\left(\frac{z\boldsymbol{e}_x}{r^3} - \frac{x\boldsymbol{e}_z}{r^3}\right) + D_1\frac{zx\boldsymbol{r}}{r^5} \\ & + E_1\left(z\boldsymbol{e}_x + x\boldsymbol{e}_z - \frac{5xz\boldsymbol{r}}{r^2}\right)\frac{1}{r^5} + F_1\left(\boldsymbol{e}_x - \frac{2z^2\boldsymbol{e}_x + x\boldsymbol{r}}{r^2} + \frac{2xz\boldsymbol{e}_z}{r^2}\right)\frac{1}{r^3} \\ & + G_1\left(\boldsymbol{e}_x - \frac{5z^2\boldsymbol{e}_x + 10xz\boldsymbol{e}_z + 13x\boldsymbol{r}}{r^2} + \frac{75xz^2\boldsymbol{r}}{r^4}\right)\frac{1}{r^3} \\ & + H_1\left(\boldsymbol{e}_x - \frac{5z^2\boldsymbol{e}_x + 10xz\boldsymbol{e}_z + 5x\boldsymbol{r}}{r^2} + \frac{35xz^2\boldsymbol{r}}{r^4}\right)\frac{1}{r^5}. \end{aligned} \tag{3.34}$$

$${}_{(1)}p_{(0)} = A_1\frac{3x}{2r^3} + D_1\frac{2xz}{r^5} + G_1\left(\frac{-30x}{r^5} + \frac{150xz^2}{r^7}\right). \tag{3.35}$$

Here, the coefficients are defined as

$$\left.\begin{gathered} A_1 = \frac{3}{4}\left(U_{sx(0)} - \alpha - \frac{\gamma}{3} - Ha(\zeta_p - \zeta_w)\right), \\ B_1 = -\frac{1}{4}\left(U_{sx(0)} - \alpha - \frac{3\gamma}{5} - Ha(\zeta_p - \zeta_w)\right) + \frac{Ha\zeta_p}{2}, \\ C_1 = \Omega_{sy(0)} - \frac{\beta}{2}, \quad D_1 = -\frac{5\beta}{2}, \quad E_1 = -\frac{\beta}{2}, \\ F_1 = \frac{\gamma}{3}, \quad G_1 = -\frac{7\gamma}{120}, \quad H_1 = \frac{\gamma}{8}. \end{gathered}\right\} \tag{3.36}$$

The terms multiplying the coefficients A_1, B_1, C_1, D_1, E_1 represent the force-monopole (stokeslet), source-dipole, antisymmetric dipole (rotlet), symmetric dipole (stresslet) and octupole singularities, respectively (Guazzelli & Morris 2011; Kim & Karrila 2013). The other disturbances (terms multiplying F_1, G_1, H_1) are further singularities in the multipole expansion which arise due to the curvature (γ) in the background flow field.

The evaluation of higher-order reflections can be found using Faxén transformation (Faxén 1922) and is identical to our previous analysis (Choudhary *et al.* 2019); the details of evaluation are provided in the supplementary material. We shall later show (in § 3.4.4) that the higher reflections of the velocity field (i.e. ${}_{(2)}\boldsymbol{v}_{(0)},\ {}_{(3)}\boldsymbol{v}_{(0)}, \ldots$) are dispensable for the current problem.

The unknown translational ($U_{sx(0)}$) and rotational ($\Omega_{sy_{(0)}}$) velocities can be evaluated using the force-free and torque-free conditions (3.24) for first three reflections (since the second reflection does not contribute to the hydrodynamic drag and torque (Happel & Brenner 2012; Kim & Karrila 2013), we evaluate the third reflection to estimate the wall corrections)

$$U_{sx(0)} = \alpha + \gamma/3 + Ha(\zeta_p - \zeta_w) + O(\kappa^2), \tag{3.37a}$$

$$\Omega_{sy(0)} = \beta/2 + O(\kappa^3). \tag{3.37b}$$

https://doi.org/10.1017/jfm.2020.397 Published online by Cambridge University Press

The $O(\kappa^2)$ and $O(\kappa^3)$ corrections are contributions from the wall reflections of the disturbance velocity, which arise when the third reflection is taken into account. The details of the derivation of (3.37) can be found in the supplementary material. Substitution of (3.37) in (3.36) yields $A_1 \sim O(\kappa^2)$, $B_1 \sim Ha\zeta_p O(1)$ and $C_1 \sim O(\kappa^3)$. Since $\kappa \ll 1$, we neglect the $O(\kappa^2)$ and $O(\kappa^3)$ wall corrections, and thus use

$$A_1 = C_1 = 0, \quad U_{sx(0)} = \alpha + \gamma/3 + Ha(\zeta_p - \zeta_w), \quad \Omega_{sy(0)} = \beta/2. \tag{3.38a–c}$$

This yields the background flow velocity in the frame of reference of $\boldsymbol{U}_{s(0)}$ (3.13),

$$\boldsymbol{U}_{\infty(0)} = \left(\beta z + \gamma z^2 - Ha\zeta_p - \frac{\gamma}{3}\right)\boldsymbol{e}_x. \tag{3.39}$$

The above estimates of A_1, C_1 and $U_{sx(0)}$ in (3.38) when substituted in (3.34) provide an insight into leading-order velocity disturbances: (i) stresslet ($\sim O(1/r^2)$ arising from the resistance to strain); (ii) source-dipole field ($\sim O(1/r^3)$ arising from the electrophoretic slip); and (iii) octupole field ($\sim O(1/r^4)$ also arising from the resistance to strain). The other disturbances (multiplying F_1, G_1, H_1), arising due to curvature in the background flow are of $O(\kappa)$ and are accounted for in the evaluation of (3.30).

3.4.4. *Evaluation of volume integral*

To estimate the migration velocity using (3.30), we substitute the velocity field $\boldsymbol{v}_{(0)}$ into the integrand. We analyse the integral for computational convenience and divide the fluid domain (V_f) into two asymptotic subdomains (Ho & Leal 1974, 1976)

$$V_1 = \{\boldsymbol{r} : 1 \leqslant |r| \leqslant \rho\}, \quad V_2 = \{\tilde{\boldsymbol{r}} : \kappa\rho \leqslant |\tilde{r}| < \infty, -s \leqslant \tilde{z} \leqslant 1 - s\}. \tag{3.40a,b}$$

Here, the intermediate radius ρ satisfies $1 \ll \rho \ll 1/\kappa$, $\tilde{r}$ represents the outer coordinates ($\tilde{r} = r\kappa$). The characteristic length scale corresponding to the inner domain (V_1) is particle radius a^*. Whereas, channel width l^* is the characteristic length corresponding to the outer domain (V_2). Below, we inspect the nature of the integrand in each subdomain and show that the integration in V_2 is not required to attain the leading-order migration velocity.

Integration in subdomain V_1: substituting (3.34) and (3.39) in (3.19) and performing the integration (3.30) in V_1 (which is essentially a spherical shell, provided the particle is not too close to the wall, i.e. $s \gg \kappa$, where $\kappa \ll 1$) (the analytical integration of the volume integral is performed using Mathematica 12; the code is provided in the supplementary material) we obtain

$$\begin{aligned}\frac{6\pi(1+O(\kappa))U^H_{mig}}{De} &= -\int_{V_1:r=1}^{r=\rho} \boldsymbol{s}_{(0)} : \nabla \boldsymbol{u}^t \,\mathrm{d}V = -\int_{V_1:r=1}^{r=\infty} \boldsymbol{s}_{(0)} : \nabla \boldsymbol{u}^t \,\mathrm{d}V + o(\kappa) \\ &\approx \frac{10\pi}{3}\beta\gamma(1+3\delta) - \frac{3\pi}{2}\beta Ha\zeta_p(1+\delta).\end{aligned} \tag{3.41}$$

The details of $o(\kappa)$ error incurred while approximating the upper limit of the integral to $r = \infty$ is detailed in appendix B.

In view of the definition of β and γ, the first term in (3.41) is $O(\kappa)$, and is identical to that obtained by Ho & Leal (1976), who reported the viscoelastic migration of a particle in the absence of electrokinetic effects. The second term is $O(1)$ and is

https://doi.org/10.1017/jfm.2020.397 Published online by Cambridge University Press

the dominant contribution to the migration in the current study. It is interesting to note that the first term arises purely from the interaction of disturbance field and the bulk flow (i.e. $\boldsymbol{w}_{(0)}^{(1)}$ and $\boldsymbol{w}_{(0)}^{(2)}$). However, the second term arises from the interactions among various disturbances (i.e. $\boldsymbol{e}_{(0)}^{(1)} \cdot \boldsymbol{e}_{(0)}^{(1)}$ and $\boldsymbol{e}_{(0)}^{(2)}$). This insight and the proportionality to $\beta Ha\zeta_p$ (second term) suggests that the $O(1)$ modification to migration arises from the interaction of stresslet and octupole disturbances (both proportional to β) with the electrophoresis induced source dipole disturbance (proportional to $Ha\zeta_p$).

Integration in subdomainV_2: we now find the contribution of the integral in the outer subdomain V_2. Since the characteristic length in the outer domain is l^*, the disturbances are stretched into the outer coordinates ($\tilde{r} = r\kappa$). In the outer coordinate representation, the order of magnitude of the leading-order disturbance and test field velocity is

$$\tilde{\boldsymbol{v}}_{(0)} \sim Ha\zeta_p O(\kappa^3) + \beta O(\kappa^2) + \beta O(\kappa^4) + \gamma O(\kappa^3) + \gamma O(\kappa^5), \tag{3.42a}$$

$$\tilde{\boldsymbol{u}}^t \sim O(\kappa) + O(\kappa^3). \tag{3.42b}$$

In the outer coordinates, the undisturbed background flow velocity is

$$\tilde{\boldsymbol{U}}_{\infty(0)} \sim \beta O(1/\kappa) + \gamma O(1/\kappa^2) + Ha\zeta_p O(1) + \gamma O(1). \tag{3.43}$$

We substitute (3.42*a*) and (3.43) in (3.19) and obtain $\tilde{\boldsymbol{s}}_{(0)}$.

The volume integral (3.30), in V_2 subdomain, is represented in outer coordinates as

$$\frac{6\pi(1+O(\kappa))U_{mig}^H}{De} = -\int_{V_2} \tilde{\boldsymbol{s}}_{(0)} : (\kappa\tilde{\boldsymbol{\nabla}}\tilde{\boldsymbol{u}}^t)\kappa^{-3}\,\mathrm{d}\tilde{V}. \tag{3.44}$$

Upon simplification, we find that the integrand is $O(\kappa^2)$. Since $\kappa \ll 1$, the dominant contribution can be concluded to arise from the inner integral (i.e. $O(1)$) and the contribution from the outer integral can be neglected. In § D.1, the expression for leading-order migration velocity (3.41) is verified using an independent calculation following the theorem of Giesekus (1963) for the special case of polymeric fluids ($\Psi_2^* = -0.5\Psi_1^*$).

4. Results and discussion

The expression for the migration velocity (3.41) shows that the direction of lateral migration is determined by the magnitude and sign of the viscometric parameter δ and De. For most viscoelastic fluids De is positive, and δ is reported to be between -0.5 and -0.7 (Caswell & Schwarz 1962; Leal 1975; Bird *et al.* 1987; Koch & Subramanian 2006). Since γ is negative, the first term in (3.41) is strictly positive below the centreline ($\beta > 0$) and negative above it ($\beta < 0$), i.e. the pure elastic stresses push the particle towards the channel axis at $O(\kappa)$. The second term is $O(1)$; its proportionality to $Ha\zeta_p$ indicates that this dominant contribution originates due to the electrophoretic slip, i.e. incorporation of electrophoresis enhances the migration by $O(\kappa^{-1})$. For $-0.7 < \delta < -0.5$, a particle with positive ζ_p will migrate towards the walls (at $O(1)$) when the electric field is applied in the direction of the flow. The reverse would hold for a particle with negative ζ_p or if the electric field is applied in the opposite direction. These findings qualitatively agree with the experimental observations depicted in figure 1.

https://doi.org/10.1017/jfm.2020.397 Published online by Cambridge University Press

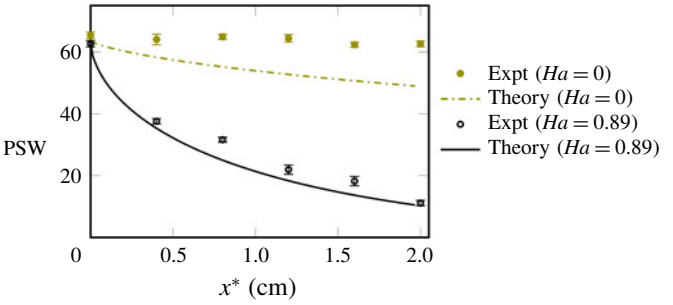


FIGURE 3. Particle stream width, PSW, (μm) of negative zeta potential particles suspended in a Poiseuille flow of second-order fluid. Parameters: $De = 0.12$; $\delta = -0.5$; $E^*_\infty = 300$ V cm^{-1}; $\zeta_p = -2.52$ ($\zeta^*_p = -83$ mV); $l^* = 66$ μm; $\kappa = 0.017$.

The enhancement demonstrates that an addition of electrokinetic slip on the particle surface can drastically alter the normal stresses which consequently enhances the particle migration. The slip creates a source-dipole disturbance in the fluid which decays rapidly away from the particle ($\sim O(1/r^3)$). This suggests that the migration occurs from short-ranged interactions, which are unaffected by the boundaries unless the particle is very close to the walls. Furthermore, equation (3.41) reveals that the parameters such as wall zeta potential (ζ_w) and curvature of the background flow (γ) do not affect the migration at the present order of approximation.

Since the experimental parameters are in the regime of the theoretical analysis ($De < 1$, $De \gg Re_p$, $Ha\zeta_p \sim O(1)$, $\kappa \ll 1$), we now quantitatively compare the two. Theoretically, the trajectories of a single particle are calculated using (3.41) and are converted to an equivalent particle stream width using $|l^* - 2(l^* - d^*)|$, for particle focusing at the centreline (l^* being the channel height and d^* is the particle to wall distance). (In § D.2, the theoretical calculation of trajectory is detailed and validated with that reported by Ho & Leal (1976) for $Ha = 0$.) We use the relaxation time scale $((\Psi_1^* + \Psi_2^*)/\mu^*)$ corresponding to $C^*_{PEO} = 250$ ppm as 2.75 ms (Lu & Xuan 2015). Figure 3 shows the comparison of particle stream widths for two cases: (i) no electric field (i.e. viscoelastic focusing) and (ii) parallel electric field (i.e. electroviscoelastic focusing). For case (i), the theoretical prediction shows modest particle migration. The experiments show negligible focusing as some particles get trapped near the channel corners, which is one of the limitations of viscoelastic focusing at low flow rates (Lu *et al.* 2017; Tian *et al.* 2019). Since our model is valid for two-dimensional flows, it does not account for the trapping of particles at three-dimensional corners. For case (ii), the theoretical predictions and experimental results confirm an order of magnitude enhancement in focusing. The trapping of particles at the corners is not seen here as the repulsive Maxwell lift is strongest near the corners (Liang, Qian & Xuan 2010). Thus, the agreement between the experiments and theoretical analysis is improved.

Our mathematical framework reveals that the migration in figure 1(*b*,*c*) arises from: (i) Maxwell stresses (3.26); (ii) pure viscoelastic stresses (3.41-term 1); and (iii) electrophoresis enhanced viscoelastic stresses (3.41-term 2). A comparison of these migration velocities, namely, Maxwell migration (MM), viscoelastic migration (VM) and electroviscoelastic migration (EVM) is shown in figure 4. The curves correspond to the case in figure 1(*b*): a particle with negative zeta potential and electric field applied parallel to the flow. The migration due to decoupled Maxwell

https://doi.org/10.1017/jfm.2020.397 Published online by Cambridge University Press

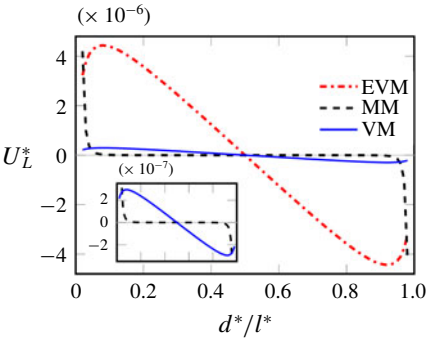


FIGURE 4. Comparison of various components of the migration velocity (m s^{-1}) for $\kappa = 0.017$; Maxwell migration, MM; viscoelastic migration, VM; and electroviscoelastic migration, EVM. Here EVM corresponds to figure 1(*b*). The inset shows the comparison of MM and VM. Parameters: $De = 0.12$; $\delta = -0.5$; $E_\infty^* = 300$ V cm^{-1}; $\zeta_p = -2.52$ ($\zeta_p^* = -83$ mV); $l^* = 66$ μm; $\kappa = 0.017$.

stresses (i.e. MM) is dominant near the walls and decays rapidly away from it. Although this wall-repulsive force is negligible in the bulk of the channel (for $\kappa \ll 1$), it helps eliminate the corner equilibrium positions (Liang *et al.* 2010). The other components VM and EVM act towards the centre as depicted by the negative gradient at the central equilibrium position. For conditions corresponding to figure 1(*c*), where flow and electric field are opposite to each other ($Ha < 0$), the EVM curve would reverse, as we can see from (3.41). As a consequence, the central equilibrium position would become unstable, resulting in particle migration towards the walls.

5. Conclusions

Our experimental and theoretical analysis depict an enhancement of $O(\kappa^{-1})$ in migration of a particle in viscoelastic flow, when subjected to a parallel electric field. Here κ is the ratio of particle radius to channel size. Using a second-order fluid model, the theoretical analysis reveals the contribution from different underlying stresses around the particle (see (3.26) and (3.41)). These constitute an approximate expression for the migration velocity which agrees well with the experimental results. The analytical results further reveal that the particle zeta potential and background shear determine the equilibrium positions. Wall zeta potential, Maxwell stresses and curvature of the background flow do not affect the migration at the leading order.

Karnis & Mason (1966) and Gauthier *et al.* (1971) suggested that the normal stresses in the undisturbed flow (i.e. tensioned streamlines) are responsible for the migration of the neutral sphere towards the channel centre. Later, Ho & Leal (1976) reported that this explanation might not be entirely accurate because of the presence of strong disturbance flow around the sphere. However, the disturbance due to a freely suspended particle in the shear flow does not exhibit a stagnation point, and thus the profile is still predominantly a shear flow (Ho & Leal 1976; Guazzelli & Morris 2011). Thus the notion of streamlined tension is not altogether lost and can be applied for a neutral particle. For the case of an electrophoretic particle, the above explanation may not hold as the characteristic disturbance field (being a source dipole) exhibits stagnation points, which should be responsible for the direction of migration addressed in this work. This intriguing feature entails a detailed, perhaps numerical,

https://doi.org/10.1017/jfm.2020.397 Published online by Cambridge University Press

description of pressure and stress fields around the electrophoretic particle to test this speculation, and warrants further investigation.

The findings of the current work have a direct practical relevance to applications related to lab-on-a-chip devices used to separate cells in biological fluids which are known to exhibit non-Newtonian behaviour (Stoecklein & Di Carlo 2018; Yuan *et al.* 2018). The current work addresses the particle migration in dilute polymer concentration regime. For higher polymer concentrations, the direction of migration is reported to be opposite to that of the current work and the explanation for this is currently unknown (Li & Xuan 2018). Several studies (Rodd *et al.* 2005; Yang *et al.* 2011; Kim *et al.* 2012) have reported that flows consisting semidilute polymer concentration regime may exhibit shear-thinning behaviour. In such cases, constitutive models like FENE-P and Giesekus fluid can be implemented numerically to accurately predict the particle migration. In our future studies we intend to explore these areas.

Acknowledgement

The financial support from Indian Ministry of Human Resource Development is gratefully acknowledged.

Declaration of interests

The authors report no conflict of interest.

Supplementary movies and material

Supplementary movies and material are available at https://doi.org/10.1017/jfm.2020.397.

Appendix A

A.1. *Evaluation of ψ using the method of reflections*

To satisfy the boundary conditions at both the particle and wall surface, we seek the disturbance potential as a sum of reflections

$$\psi = {}_{(1)}\psi + {}_{(2)}\psi + \cdots. \tag{A 1}$$

Here, ${}_{(i)}\psi$ represents the ith reflection. The odd reflections satisfy boundary conditions at the particle surface and even reflections satisfy wall boundary conditions. Substituting the above equation in the Laplace equation ($\nabla^2\psi = 0$), we obtain for the first reflection

$$\left.\begin{array}{c} \nabla^2\, {}_{(1)}\psi = 0, \\ \boldsymbol{e}_r \cdot \boldsymbol{\nabla}\, {}_{(1)}\psi = -\boldsymbol{e}_r \cdot \boldsymbol{\nabla}\phi_\infty \quad \text{at } r = 1, \\ {}_{(1)}\psi \to 0 \quad \text{as } r \to \infty, \end{array}\right\} \tag{A 2}$$

and for the second reflection

$$\left.\begin{array}{c} \nabla^2\, {}_{(2)}\psi = 0, \\ \boldsymbol{e}_z \cdot \boldsymbol{\nabla}\, {}_{(2)}\psi = -\boldsymbol{e}_z \cdot \boldsymbol{\nabla}\, {}_{(1)}\psi \quad \text{at walls.} \end{array}\right\} \tag{A 3}$$

Solution to ${}_{(1)}\psi$: equation (A 2) suggests that ${}_{(1)}\psi$ is a harmonic function which decays as $r \to \infty$. The boundary condition suggests that it must be linear in the

https://doi.org/10.1017/jfm.2020.397 Published online by Cambridge University Press

'driving force', $\nabla\phi_\infty(=-\boldsymbol{e}_x)$. Therefore, the solution is sought in terms of spherical solid harmonics (Guazzelli & Morris 2011) as

$$_{(1)}\psi = \frac{1}{2}\frac{\boldsymbol{r}}{r^3}\cdot\nabla\phi_\infty = -\frac{1}{2}\frac{x}{r^3}. \tag{A 4}$$

Solution to $_{(2)}\psi$: to evaluate $_{(2)}\psi$, we adopt the approach devised by Faxén (1922) in the context of bounded viscous flows. Using this, the disturbance around the particle is expressed in an integral form which satisfies the boundary conditions at the walls. The first reflection is characterized by particle scale (a^*). The second reflection $_{(2)}\psi$ is characterized by a length scale l^*. Therefore, the coordinates for second reflection are stretched, and are termed as 'outer' coordinates. These outer coordinates (denoted by tilde) are defined as

$$\tilde{r} = r\kappa, \quad \tilde{x} = x\kappa, \quad \tilde{y} = y\kappa, \quad \tilde{z} = z\kappa. \tag{A 5a–d}$$

Since $_{(2)}\psi$ depends on $_{(1)}\psi$ through the wall boundary condition in (A 3), both reflections must be represented in the coordinates of same scale. The first reflection of potential disturbance in the outer coordinates ($_{(1)}\tilde{\psi}$) is represented as

$$_{(1)}\tilde{\psi} = -\frac{1}{2}\frac{\tilde{x}}{\tilde{r}^3}\kappa^2. \tag{A 6}$$

Faxén (1922) represented the fundamental solution of the Laplace equation (in Cartesian space) in the terms of Fourier integrals as

$$\frac{1}{\tilde{r}} = \frac{1}{2\pi}\int_{-\infty}^{+\infty}\int_{-\infty}^{+\infty} \mathrm{e}^{(\mathrm{i}\Theta-(\lambda|\tilde{z}|/2))}\frac{\mathrm{d}\xi\,\mathrm{d}\eta}{2\lambda}. \tag{A 7}$$

Here, $\Theta = (\xi\tilde{x} + \eta\tilde{y})/2$ and $\lambda = (\xi^2+\eta^2)^{1/2}$ where ξ and η are the variables in Fourier space. We transform the disturbance field (A 6) by taking derivatives of the above (A 7). For example, equation (A 6) contains $\tilde{x}/\tilde{r}^3$, which is expressed using the above transformation as

$$\frac{\tilde{x}}{\tilde{r}^3} = -\frac{\partial}{\partial\tilde{x}}\left(\frac{1}{\tilde{r}}\right) = \frac{1}{2\pi}\int_{-\infty}^{+\infty}\int_{-\infty}^{+\infty} \mathrm{e}^{(\mathrm{i}\Theta-(\lambda|\tilde{z}|/2))}\left(-\frac{\mathrm{i}\xi}{2}\right)\frac{\mathrm{d}\xi\,\mathrm{d}\eta}{2\lambda}. \tag{A 8}$$

This yields an integral representation for the first reflection

$$_{(1)}\tilde{\psi} = \frac{\kappa^2}{2\pi}\int_{-\infty}^{+\infty}\int_{-\infty}^{+\infty} \mathrm{e}^{(\mathrm{i}\Theta-(\lambda|\tilde{z}|/2))}b_1\left(\frac{\mathrm{i}\xi}{\lambda}\right)\mathrm{d}\xi\,\mathrm{d}\eta. \tag{A 9}$$

Here, $b_1 = 1/8$. The boundary condition expressed in (A 3) suggests a form of solution for $_{(2)}\tilde{\psi}$ similar to the above equation,

$$_{(2)}\tilde{\psi} = \frac{\kappa^2}{2\pi}\int_{-\infty}^{+\infty}\int_{-\infty}^{+\infty} \mathrm{e}^{\mathrm{i}\Theta}(\mathrm{e}^{(-\lambda\tilde{z}/2)}b_2 + \mathrm{e}^{(+\lambda\tilde{z}/2)}b_3)\left(\frac{\mathrm{i}\xi}{\lambda}\right)\mathrm{d}\xi\,\mathrm{d}\eta. \tag{A 10}$$

Substituting (A 9) and (A 10) in the boundary condition (A 3), yields b_2 and b_3 in terms of b_1

$$b_2 = \frac{b_1(1+\mathrm{e}^{(1-s)\lambda})}{-1+\mathrm{e}^{\lambda}}, \quad b_3 = \frac{b_1(1+\mathrm{e}^{s\lambda})}{-1+\mathrm{e}^{\lambda}}. \tag{A 11a,b}$$

The next reflection ($_{(3)}\psi$) is $O(\kappa^3)$. As we restrict $\kappa \ll 1$, the first two reflections capture the leading-order contribution to the disturbance potential.

https://doi.org/10.1017/jfm.2020.397 Published online by Cambridge University Press

A.2. *Evaluation of Maxwell migration*

The electric force and torque are expressed as a function of reflections as

$$\boldsymbol{F}_M = 4\pi Ha \int_{S_p} \boldsymbol{n} \cdot \begin{pmatrix} \boldsymbol{\nabla}({}_{(1)}\psi + {}_{(2)}\psi)\boldsymbol{\nabla}({}_{(1)}\psi + {}_{(2)}\psi) \\ -\frac{1}{2}(\boldsymbol{\nabla}({}_{(1)}\psi + {}_{(2)}\psi) \cdot \boldsymbol{\nabla}({}_{(1)}\psi + {}_{(2)}\psi))\boldsymbol{I} \end{pmatrix} \mathrm{d}S, \tag{A 12}$$

$$\boldsymbol{L}_M = 4\pi Ha \int_{S_p} \boldsymbol{n} \times \left(\boldsymbol{n} \cdot \begin{pmatrix} \boldsymbol{\nabla}({}_{(1)}\psi + {}_{(2)}\psi)\boldsymbol{\nabla}({}_{(1)}\psi + {}_{(2)}\psi) \\ -\frac{1}{2}(\boldsymbol{\nabla}({}_{(1)}\psi + {}_{(2)}\psi) \cdot \boldsymbol{\nabla}({}_{(1)}\psi + {}_{(2)}\psi))\boldsymbol{I} \end{pmatrix} \right) \mathrm{d}S. \tag{A 13}$$

The gradient of first reflection ($\boldsymbol{\nabla}_{(1)}\psi$) at the particle surface is

$$\boldsymbol{\nabla}_{(1)}\psi|_{r=1} = \tfrac{1}{2}\{-1 + 3\sin^2\theta\cos^2\varphi,\ 3\sin^2\theta\sin\varphi\cos\varphi,\ 3\sin\theta\cos\theta\cos\varphi\}. \tag{A 14}$$

Here, φ and θ denote the azimuthal and polar angle, respectively. As the wall reflection of the potential is represented in the outer-scaled coordinates, $\boldsymbol{\nabla}_{(2)}\psi$ at the particle surface ($r = 1$) is expressed as a Taylor series expansion of $\kappa\tilde{\boldsymbol{\nabla}}\tilde{\psi}_2$ about the origin ($\tilde{r} \to 0$). Here $\tilde{\boldsymbol{\nabla}}$ is the spatial gradient in outer-scaled coordinates, $\{\partial/\partial\tilde{x}, \partial/\partial\tilde{y}, \partial/\partial\tilde{z}\}$. Since the particle is small with respect to the wall–particle gap ($\kappa/s \ll 1$), we retain only the zeroth and first-order terms

$$\boldsymbol{\nabla}_{(2)}\psi|_{r=1} = \int_0^\infty \begin{bmatrix} \kappa^3(-(b_2+b_3)\lambda^2/4)\{1,0,0\} \\ +\kappa^4((b_2-b_3)\lambda^3/8)\{1,0,1\} \end{bmatrix} \mathrm{d}\lambda + O(\kappa^5). \tag{A 15}$$

Substituting ${}_{(1)}\psi$ and ${}_{(2)}\psi$ in both (A 12) and (A 13) and using (A 14) and (A 15), we obtain

$$\boldsymbol{F}_M = 4\pi Ha \left(\frac{3\pi}{16}\kappa^4(\mathfrak{Z}(4,s) - \mathfrak{Z}(4,1-s)) \right) \boldsymbol{e}_z + O(\kappa^7) \quad \text{and} \quad \boldsymbol{L}_M = \boldsymbol{0}. \tag{A 16a,b}$$

Appendix B. Test field ($\boldsymbol{u}^t$)

The test field is chosen to be that generated by a sphere moving in the positive z-direction with a unit velocity in a quiescent Newtonian medium

$$\left.\begin{array}{c} \boldsymbol{\nabla}\cdot\boldsymbol{u}^t = 0, \quad \nabla^2\boldsymbol{u}^t - \boldsymbol{\nabla}p^t = \boldsymbol{0}, \\ \boldsymbol{u}^t = \boldsymbol{e}_z \quad \text{at } r = 1, \\ \boldsymbol{u}^t = \boldsymbol{0} \quad \text{at the walls}, \\ \boldsymbol{u}^t \to \boldsymbol{0} \quad \text{at } r \to \infty. \end{array}\right\} \tag{B 1}$$

To solve for $\boldsymbol{u}^t$, we again make use of the fact that the integration in V_1 is sufficient for the leading-order solution and solve for the first reflection of $\boldsymbol{u}^t$ using Lamb's solution

$${}_{(1)}\boldsymbol{u}^t = \frac{3}{4}\left(\boldsymbol{e}_z + \frac{z\boldsymbol{r}}{r^2}\right)\frac{1}{r} + \frac{1}{4}\left(\boldsymbol{e}_z - \frac{3z\boldsymbol{r}}{r^2}\right)\frac{1}{r^3}. \tag{B 2}$$

Appendix C

Here we analyse the integrand of (3.30) in subdomain $V_1 = \{\boldsymbol{r} : 1 \leqslant |r| \leqslant \rho\}$, where ρ is an intermediate radius ($1 \ll \rho \ll \kappa^{-1}$). The order of magnitude of the leading-order disturbance and test field velocity are

$$\boldsymbol{v}_{(0)} \sim Ha\zeta_p O(1/r^3) + \beta O(1/r^2) + \beta O(1/r^4) + \gamma O(1/r^3) + \gamma O(1/r^5) \quad \text{and} \tag{C 1a}$$

$$\boldsymbol{u}^t \sim O(1/r) + O(1/r^3). \tag{C 1b}$$

https://doi.org/10.1017/jfm.2020.397 Published online by Cambridge University Press

From (3.39), we obtain the order of magnitude of the undisturbed velocity

$$\boldsymbol{U}_{\infty(0)} \sim \beta O(r) + \gamma O(r^2) + Ha\zeta_p O(1) + \gamma O(1). \tag{C 2}$$

We substitute (C 1) and (C 2) in (3.19) and use it in (3.30) to find the order of magnitude of integrand $\boldsymbol{s}_{(0)} : \nabla \boldsymbol{u}^t$ in V_1

$$\begin{aligned} &= (Ha\zeta_p)^2 O\left(\frac{1}{r^{10}} + \delta\frac{1}{r^7} + \cdots\right) \\ &\quad + \beta Ha\zeta_p O\left(\frac{1}{r^6} + \delta\frac{1}{r^6} + \cdots\right) + \gamma Ha\zeta_p O\left(\frac{1}{r^5} + \delta\frac{1}{r^5} + \cdots\right) \\ &\quad + \beta^2 O\left(\frac{1}{r^5} + \delta\frac{1}{r^5} + \cdots\right) + \beta\gamma O\left(\frac{1}{r^4} + \delta\frac{1}{r^6} + \cdots\right) + \gamma^2 O\left(\frac{1}{r^5} + \delta\frac{1}{r^5} + \cdots\right). \end{aligned} \tag{C 3}$$

The coefficients of different terms in (C 3) depict contributions to the integrand arising from various interactions. The radial order describes the range of interaction. Equation (3.41) suggests that the contribution from all the terms in (C 3) vanish except the second and fifth term.

We now analyse the error associated with the approximation of the upper limit of integral as $r = \infty$ in (3.41). Following Ho & Leal (1974), the intermediate radius ρ is written as

$$\rho \sim O(\kappa^{\eta-1}), \quad \text{where } 0 < \eta < 1. \tag{C 4}$$

Out of the two non-vanishing components of integrand in (C 3), the fifth term decays the slowest $\sim O(1/r^4)$. Thus, the leading-order error is generated due to it. Its contribution to the integral $(\int_{V_1} \boldsymbol{s}_0 : \nabla \boldsymbol{u}^t \,\mathrm{d}V)$ is

$$\begin{aligned} &= \int_{V_1:r=1}^{r=\rho\sim O(\kappa^{\eta-1})} \beta\gamma O\left(\frac{1}{r^4} + \delta\frac{1}{r^6} + \cdots\right) r^2 \sin\theta \,\mathrm{d}\varphi \,\mathrm{d}\theta \,\mathrm{d}r \\ &= \beta\gamma\ O\left(\frac{1}{r} + \delta\frac{1}{r^3} + \cdots\right)\Bigg|_{r=1}^{r=\rho\sim O(\kappa^{\eta-1})} \\ &= \beta\gamma\ O\left(\frac{1}{r} + \delta\frac{1}{r^3} + \cdots\right)\Bigg|_{r=1}^{r=\infty} + \beta\gamma O\left(\frac{1}{\kappa^{\eta-1}}\right). \end{aligned} \tag{C 5}$$

Using the definitions in (3.15), we conclude that the error incurred above is $O(\kappa^{2-\eta})$. For $0 < \eta < 1$ and $1 \ll \rho \ll \kappa^{-1}$, the error is $o(\kappa)$.

Appendix D

D.1. *Validation using the three-dimensional Giesekus theorem*

For a special case of $\delta = -1$ (corresponding to $\Psi_2^* = -0.5\Psi_1^*$), Giesekus theorem (Giesekus 1963; Bird *et al.* 1987) states that the velocity in a second-order fluid is unaltered from the Newtonian velocity. However, the steady pressure field alters as

$$P = P_{(0)} + De\delta\left(\boldsymbol{U}_{(0)} \cdot \nabla P_{(0)} + \tfrac{1}{4}(\boldsymbol{E}^{(1)}_{(0)} : \boldsymbol{E}^{(1)}_{(0)})\right). \tag{D 1}$$

We substitute the Newtonian velocity and pressure field and evaluate the modified pressure. This pressure is now substituted in the total hydrodynamic stress tensor $\boldsymbol{T} = -P\boldsymbol{I} + \boldsymbol{E}^{(1)} + De\boldsymbol{S}$. The polymeric stress ($\boldsymbol{S}$) can be represented as an addition of the

https://doi.org/10.1017/jfm.2020.397 Published online by Cambridge University Press

corotational derivative ($\boldsymbol{S}_C$) and quadratic component ($\boldsymbol{S}_Q$) of the rate of strain tensor (Koch & Subramanian 2006)

$$\boldsymbol{S}_Q = (1+\delta)(\boldsymbol{E}^{(1)}\cdot\boldsymbol{E}^{(1)}) \quad \text{and} \quad \boldsymbol{S}_C = \delta\left(\frac{\partial \boldsymbol{E}^{(1)}}{\partial t} + \boldsymbol{U}\cdot\nabla\boldsymbol{E}^{(1)} + \tfrac{1}{2}(\boldsymbol{R}^{(1)}\cdot\boldsymbol{E}^{(1)} + \boldsymbol{E}^{(1)}\cdot\boldsymbol{R}^{(1)\dagger})\right), \tag{D 2a,b}$$

where $\boldsymbol{R}^{(1)}$ is the rate of rotation tensor ($\nabla\boldsymbol{U} - \nabla\boldsymbol{U}^{\dagger}$). In the limit of $\delta = -1$, the quadratic stress vanishes.

Accounting for the leading-order effects of viscoelasticity on the lateral force (provided $\delta = -1$) yields

$$De\boldsymbol{F}_{(1)} = \int_S De\boldsymbol{T}_{(1)}\cdot\boldsymbol{n}\,\mathrm{d}S = \int_S De(-P_{(1)}\boldsymbol{I} + \boldsymbol{S}_{C(0)})\cdot\boldsymbol{n}\,\mathrm{d}S. \tag{D 3}$$

Here, $\boldsymbol{n}$ is the unit normal vector pointing outside the sphere and $\boldsymbol{S}_{C(0)}$ is evaluated by substituting the Newtonian field ($\boldsymbol{U}_{(0)}, P_{(0)}$) in (D 2). Solving the above integral results in the following lateral force:

$$De\boldsymbol{F}_{(1)} = De\left(-\frac{20\pi}{3}\beta\gamma\right)\boldsymbol{e}_z, \tag{D 4}$$

which is identical to that obtained from (3.41) for $\delta = -1$. In the above calculation, $De\delta(-(24\pi/3)\beta\gamma - 12\pi\beta Ha\zeta_p)$ is the contribution from pressure field, and $De\delta((44\pi/3)\beta\gamma + 12\pi\beta Ha\zeta_p)$ is the contribution from the corotational stress. The analysis here shows that the enhancement in migration comes entirely from the quadratic stress.

D.2. *Evaluation and validation of the particle trajectory*

The ratio of migration velocity to the translational velocity is

$$\frac{U_{mig}}{U_{sx}} = \frac{\mathrm{d}s/\mathrm{d}t}{\mathrm{d}x/\mathrm{d}t} = \frac{\mathrm{d}s}{\mathrm{d}x}. \tag{D 5}$$

At the leading order, U_{sx} can be approximated as $U_{sx(0)}$ because the corrections arrive at $O(De)$ (due to weak non-Newtonian effects) and $O(\kappa^2)$ (due to wall induced viscous resistance). Here, U_{mig} has both hydrodynamic and Maxwell stress contributions (i.e. $U^H_{mig} + U^M_{mig}$). Using the first-order Euler method and substituting U^H_{mig}, U^M_{mig} and $U_{sx(0)}$, we obtain the equation governing the particle trajectory

$$\begin{aligned} s^{n+1} &\approx s^n + \Delta x\left(\frac{U^H_{mig} + U^M_{mig}}{U_{sx(0)}}\right) \\ &\approx s^n + \Delta x\left[\frac{De\left(\frac{10\pi}{3}\beta\gamma(1+3\delta) - \frac{3\pi}{2}\beta Ha\zeta_p(1+\delta)\right) + 4\pi Ha\left(\frac{3\pi}{16}\kappa^4(\mathfrak{Z}(4,s) - \mathfrak{Z}(4,1-s))\right)}{6\pi(1+O(\kappa))\left(\alpha + \frac{\gamma}{3} + Ha(\zeta_p - \zeta_w)\right)}\right]. \end{aligned} \tag{D 6}$$

Since $\alpha \sim O(\kappa^{-1})$, $\gamma \sim O(\kappa)$, $Ha(\zeta_p - \zeta_w) \sim O(1)$, the trajectory equation can be approximately represented as

$$\begin{aligned} s^{n+1} \approx\ & s^n + \frac{\Delta x}{6\pi(1+O(\kappa))\alpha}\left[De\left(\frac{10\pi}{3}\beta\gamma(1+3\delta) - \frac{3\pi}{2}\beta Ha\zeta_p(1+\delta)\right)\right. \\ & \left. + 4\pi Ha\left(\frac{3\pi}{16}\kappa^4(\mathfrak{Z}(4,s) - \mathfrak{Z}(4,1-s))\right)\right]. \end{aligned} \tag{D 7}$$

https://doi.org/10.1017/jfm.2020.397 Published online by Cambridge University Press

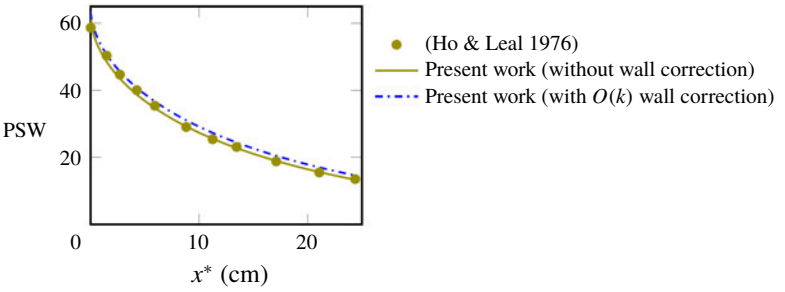


FIGURE 5. Comparison with Ho & Leal (1976): particle stream width (μm) of electrically neutral particles ($\zeta_p = 0$), suspended in a viscoelastic flow. Parameters: $De = 0.12$; $\delta = -0.5$; $l^* = 66$ μm; $\kappa = 0.017$.

We convert this trajectory into an equivalent particle stream width (PSW) for the case of centreline migration (figure 1*b*). Since the concentration of suspension is dilute (<0.1 % in volume fraction), we neglect particle–particle interactions. At the inlet, particles are homogeneously suspended and cover the entire width of the channel. As the suspension flows, the particles migrate towards the centreline.

Experimentally, PSW is measured by tracking the spread of particles (i.e. for centreline focusing, the particle closest to the walls is tracked). Theoretically, using (D 7), we find the trajectory of this particle, which is initially suspended near the wall ($s^1 = 0.95$). The non-dimensional PSW associated with this trajectory is evaluated using $|1 - 2(1 - s^n)|$. For instance, $s^n = 0.8$ or 0.2 corresponds to $PSW = 0.6$, i.e. the dilute suspension of particles cover 60 % of the channel width. In dimensional form, the particle stream width is $|l^* - 2(l^* - d^{*n})|$. Figure 5 depicts the stream width of particles suspended in a pressure driven flow of second-order fluid, in the absence of an electric field. The result matches well with that reported by Ho & Leal (1976, p. 796) (the trajectories are converted to PSW using $|l^* - 2(l^* - d^{*n})|$). The dashed line shows the particle stream width when wall effects are taken into account (at the leading order). Results in § 4 include this first-order wall correction.

REFERENCES

ANDERSON, J. L. 1989 Colloid transport by interfacial forces. *Annu. Rev. Fluid Mech.* **21** (1), 61–99.

BECKER, L. E., MCKINLEY, G. H. & STONE, H. A. 1996 Sedimentation of a sphere near a plane wall: weak non-Newtonian and inertial effects. *J. Non-Newtonian Fluid Mech.* **63** (2–3), 201–233.

BIRD, R. B., ARMSTRONG, R. C. & HASSAGER, O. 1987 *Dynamics of Polymeric Liquids, Vol. 1: Fluid Mechanics*. Wiley.

BRENNER, H. 1961 The slow motion of a sphere through a viscous fluid towards a plane surface. *Chem. Engng Sci.* **16** (3–4), 242–251.

BRENNER, H. 1962 Effect of finite boundaries on the Stokes resistance of an arbitrary particle. *J. Fluid Mech.* **12** (1), 35–48.

CASWELL, B. & SCHWARZ, W. H. 1962 The creeping motion of a non-Newtonian fluid past a sphere. *J. Fluid Mech.* **13** (3), 417–426.

CHEN, B., LE, W., WANG, Y., LI, Z., WANG, D., REN, L., LIN, L., CUI, S., HU, J. J., HU, Y. *et al.* 2016 Targeting negative surface charges of cancer cells by multifunctional nanoprobes. *Theranostics* **6** (11), 1887–1898.

https://doi.org/10.1017/jfm.2020.397 Published online by Cambridge University Press

CHOUDHARY, A., RENGANATHAN, T. & PUSHPAVANAM, S. 2019 Inertial migration of an electrophoretic rigid sphere in a two-dimensional Poiseuille flow. *J. Fluid Mech.* **874**, 856–890.

DATT, C., NATALE, G., HATZIKIRIAKOS, S. G. & ELFRING, G. J. 2017 An active particle in a complex fluid. *J. Fluid Mech.* **823**, 675–688.

D'AVINO, G., GRECO, F. & MAFFETTONE, P. L. 2017 Particle migration due to viscoelasticity of the suspending liquid and its relevance in microfluidic devices. *Annu. Rev. Fluid Mech.* **49**, 341–360.

DI CARLO, D. 2009 Inertial microfluidics. *Lab on a Chip* **9** (21), 3038–3046.

FAXÉN, H. 1922 The resistance to the movement of a rigid sphere in a zippered liquid enclosed between two parallel plane *w*. *Ann. Phys.* **373** (10), 89–119.

GAUTHIER, F., GOLDSMITH, H. L. & MASON, S. G. 1971 Particle motions in non-Newtonian media. II. Poiseuille flow. *Trans. Soc. Rheol.* **15** (2), 297–330.

GHOSH, U., CHAUDHURY, K. & CHAKRABORTY, S. 2016 Electroosmosis over non-uniformly charged surfaces: modified Smoluchowski slip velocity for second-order fluids. *J. Fluid Mech.* **809**, 664–690.

GIESEKUS, H. 1963 Die simultane translations-und rotationsbewegung einer kugel in einer elastoviskosen flüssigkeit. *Rheol. Acta* **3** (1), 59–71.

GUAZZELLI, E. & MORRIS, J. F. 2011 *A Physical Introduction to Suspension Dynamics*, vol. 45. Cambridge University Press.

HAPPEL, J. & BRENNER, H. 2012 *Low Reynolds Number Hydrodynamics: With Special Applications to Particulate Media*, vol. 1. Springer Science and Business Media.

HO, B. P. & LEAL, L. G. 1974 Inertial migration of rigid spheres in two-dimensional unidirectional flows. *J. Fluid Mech.* **65** (2), 365–400.

HO, B. P. & LEAL, L. G. 1976 Migration of rigid spheres in a two-dimensional unidirectional shear flow of a second-order fluid. *J. Fluid Mech.* **76** (4), 783–799.

KARNIS, A. & MASON, S. G. 1966 Particle motions in sheared suspensions. XIX. Viscoelastic media. *Trans. Soc. Rheol.* **10** (2), 571–592.

KEH, H.-J. & ANDERSON, J. L. 1985 Boundary effects on electrophoretic motion of colloidal spheres. *J. Fluid Mech.* **153**, 417–439.

KIM, B. & KIM, J. M. 2016 Elasto-inertial particle focusing under the viscoelastic flow of dna solution in a square channel. *Biomicrofluidics* **10** (2), 024111.

KIM, J. Y., AHN, S. W., LEE, S. S. & KIM, J. M. 2012 Lateral migration and focusing of colloidal particles and dna molecules under viscoelastic flow. *Lab on a Chip* **12** (16), 2807–2814.

KIM, S. & KARRILA, S. J. 2013 *Microhydrodynamics: Principles and Selected Applications*. Courier Corporation.

KOCH, D. L. & SUBRAMANIAN, G. 2006 The stress in a dilute suspension of spheres suspended in a second-order fluid subject to a linear velocity field. *J. Non-Newtonian Fluid Mech.* **138** (2–3), 87–97.

LAMB, H. 1975 *Hydrodynamics*, 6th edn. Cambridge University Press.

LE, W., CHEN, B., CUI, Z., LIU, Z. & SHI, D. 2019 Detection of cancer cells based on glycolytic-regulated surface electrical charges. *Biophys. Rep.* **5** (1), 10–18.

LEAL, L. G. 1975 The slow motion of slender rod-like particles in a second-order fluid. *J. Fluid Mech.* **69** (2), 305–337.

LESHANSKY, A. M., BRANSKY, A., KORIN, N. & DINNAR, U. 2007 Tunable nonlinear viscoelastic focusing in a microfluidic device. *Phys. Rev. Lett.* **98** (23), 234501.

LI, D. & XUAN, X. 2018 Electrophoretic slip-tuned particle migration in microchannel viscoelastic fluid flows. *Phys. Rev. Fluids* **3** (7), 074202.

LIANG, L., QIAN, S. & XUAN, X. 2010 Three-dimensional electrokinetic particle focusing in a rectangular microchannel. *J. Colloid Interface Sci.* **350** (1), 377–379.

LU, X., LIU, C., HU, G. & XUAN, X. 2017 Particle manipulations in non-Newtonian microfluidics: a review. *J. Colloid Interface Sci.* **500**, 182–201.

LU, X. & XUAN, X. 2015 Elasto-inertial pinched flow fractionation for continuous shape-based particle separation. *Analyt. Chem.* **87** (22), 11523–11530.

https://doi.org/10.1017/jfm.2020.397 Published online by Cambridge University Press

NAM, J., TAN, J. K. S., KHOO, B. L., NAMGUNG, B., LEO, H. L., LIM, C. T. & KIM, S. 2015 Hybrid capillary-inserted microfluidic device for sheathless particle focusing and separation in viscoelastic flow. *Biomicrofluidics* **9** (6), 064117.

RODD, L. E., SCOTT, T. P., BOGER, D. V., COOPER-WHITE, J. J. & MCKINLEY, G. H. 2005 The inertio-elastic planar entry flow of low-viscosity elastic fluids in micro-fabricated geometries. *J. Non-Newtonian Fluid Mech.* **129** (1), 1–22.

ROSSI, M., MARIN, A., CEVHERI, N., KÄHLER, C. J. & YODA, M. 2019 Particle distribution and velocity in electrokinetically induced banding. *Microfluid Nanofluid* **23** (5), 67.

SMOLUCHOWSKI, M. 1903 Contribution à la théorie de l'endosmose électrique et de quelques phénomènes corrélatifs. *Bull. Akad. Sci. Cracovie.* **8**, 182–200.

STOECKLEIN, D. & DI CARLO, D. 2018 Nonlinear microfluidics. *Analyt. Chem.* **91** (1), 296–314.

SZE, A., ERICKSON, D., REN, L. & LI, D. 2003 Zeta-potential measurement using the Smoluchowski equation and the slope of the current–time relationship in electroosmotic flow. *J. Colloid Interface Sci.* **261** (2), 402–410.

TIAN, F., FENG, Q., CHEN, Q., LIU, C., LI, T. & SUN, J. 2019 Manipulation of bio-micro/nanoparticles in non-Newtonian microflows. *Microfluid Nanofluid* **23** (5), 68.

WARKIANI, M. E., TAY, A. K. P., GUAN, G. & HAN, J. 2015 Membrane-less microfiltration using inertial microfluidics. *Sci. Rep.* **5**, 11018.

YANG, S., KIM, J. Y., LEE, S. J., LEE, S. S. & KIM, J. M. 2011 Sheathless elasto-inertial particle focusing and continuous separation in a straight rectangular microchannel. *Lab on a Chip* **11** (2), 266–273.

YARIV, E. 2006 'Force-free' electrophoresis? *Phys. Fluids* **18** (3), 031702.

YUAN, D., ZHAO, Q., YAN, S., TANG, S.-Y., ALICI, G., ZHANG, J. & LI, W. 2018 Recent progress of particle migration in viscoelastic fluids. *Lab on a Chip* **18** (4), 551–567.

ZHANG, J., YAN, S., ALICI, G., NGUYEN, N.-T., DI CARLO, D. & LI, W. 2014 Real-time control of inertial focusing in microfluidics using dielectrophoresis (dep). *RSC Adv.* **4** (107), 62076–62085.

ZHANG, J., YAN, S., YUAN, D., ALICI, G., NGUYEN, N.-T., WARKIANI, M. E. & LI, W. 2016 Fundamentals and applications of inertial microfluidics: a review. *Lab on a Chip* **16** (1), 10–34.

https://doi.org/10.1017/jfm.2020.397 Published online by Cambridge University Press